Aluminum plasmonic metamaterials for structural color printing

Fei Cheng,[1] Jie Gao,[1,3] Liliana Stan,[2] Daniel Rosenmann,[2] David Czaplewski,[2] and Xiaodong Yang[1,*]

[1]*Department of Mechanical and Aerospace Engineering, Missouri University of Science and Technology, Rolla, Missouri 65409, USA*
[2]*Center for Nanoscale Materials, Argonne National Laboratory, Argonne, Illinois 60439, USA*
[3]*gaojie@mst.edu*
[*]*yangxia@mst.edu*

Abstract: We report a structural color printing platform based on aluminum plasmonic metamaterials supporting near perfect light absorption and narrow-band spectral response tunable across the visible spectrum to realize high-resolution, angle-insensitive color printing with high color purity and saturation. Additionally, the fabricated metamaterials can be protected by a transparent polymer thin layer for ambient use with further improved color performance. The demonstrated structural color printing with aluminum plasmonic metamaterials offers great potential for relevant applications such as security marking and information storage.

OCIS codes: (050.6624) Subwavelength structures; (240.6680) Surface plasmons; (160.3918) Metamaterials; (330.1690) Color.

References and links

1. K. Chung, S. Yu, C.-J. Heo, J. W. Shim, S.-M. Yang, M. G. Han, H.-S. Lee, Y. Jin, S. Y. Lee, N. Park, and J. H. Shin, "Flexible, angle-independent, structural color reflectors inspired by morpho butterfly wings," Adv. Mater. **24**(18), 2375–2379 (2012).
2. A. F. Kaplan, T. Xu, and L. Jay Guo, "High efficiency resonance-based spectrum filters with tunable transmission bandwidth fabricated using nanoimprint lithography," Appl. Phys. Lett. **99**(14), 143111 (2011).
3. D. Inoue, A. Miura, T. Nomura, H. Fujikawa, K. Sato, N. Ikeda, D. Tsuya, Y. Sugimoto, and Y. Koide, "Polarization independent visible color filter comprising an aluminum film with surface-plasmon enhanced transmission through a subwavelength array of holes," Appl. Phys. Lett. **98**(9), 093113 (2011).
4. T. Xu, H. Shi, Y.-K. Wu, A. F. Kaplan, J. G. Ok, and L. J. Guo, "Structural Colors: From plasmonic to carbon nanostructures," Small **7**(22), 3128–3136 (2011).
5. A. S. Roberts, A. Pors, O. Albrektsen, and S. I. Bozhevolnyi, "Subwavelength plasmonic color printing protected for ambient use," Nano Lett. **14**(2), 783–787 (2014).
6. S. J. Tan, L. Zhang, D. Zhu, X. M. Goh, Y. M. Wang, K. Kumar, C.-W. Qiu, and J. K. W. Yang, "Plasmonic color palettes for photorealistic printing with aluminum nanostructures," Nano Lett. **14**(7), 4023–4029 (2014).
7. J. S. Clausen, E. Højlund-Nielsen, A. B. Christiansen, S. Yazdi, M. Grajower, H. Taha, U. Levy, A. Kristensen, and N. A. Mortensen, "Plasmonic metasurfaces for coloration of plastic consumer products," Nano Lett. **14**(8), 4499–4504 (2014).
8. T. Xu, Y.-K. Wu, X. Luo, and L. J. Guo, "Plasmonic nanoresonators for high-resolution colour filtering and spectral imaging," Nat. Commun. **1**(5), 59 (2010).
9. K. Kumar, H. Duan, R. S. Hegde, S. C. W. Koh, J. N. Wei, and J. K. W. Yang, "Printing colour at the optical diffraction limit," Nat. Nanotechnol. **7**(9), 557–561 (2012).
10. Y.-K. R. Wu, A. E. Hollowell, C. Zhang, and L. J. Guo, "Angle-insensitive structural colours based on metallic nanocavities and coloured pixels beyond the diffraction limit," Sci. Rep. **3**, 1194 (2013).
11. B. Zeng, Y. Gao, and F. J. Bartoli, "Ultrathin nanostructured metals for highly transmissive plasmonic subtractive color filters," Sci. Rep. **3**, 2840 (2013).
12. G. Si, Y. Zhao, J. Lv, M. Lu, F. Wang, H. Liu, N. Xiang, T. J. Huang, A. J. Danner, J. Teng, and Y. J. Liu, "Reflective plasmonic color filters based on lithographically patterned silver nanorod arrays," Nanoscale **5**(14), 6243–6248 (2013).
13. J. Zhang, J.-Y. Ou, N. Papasimakis, Y. Chen, K. F. Macdonald, and N. I. Zheludev, "Continuous metal plasmonic frequency selective surfaces," Opt. Express **19**(23), 23279–23285 (2011).
14. B. Y. Zheng, Y. Wang, P. Nordlander, and N. J. Halas, "Color-selective and CMOS-compatible photodetection based on aluminum plasmonics," Adv. Mater. **26**(36), 6318–6323 (2014).

15. V. R. Shrestha, S.-S. Lee, E.-S. Kim, and D.-Y. Choi, "Aluminum plasmonics based highly transmissive polarization-independent subtractive color filters exploiting a nanopatch array," Nano Lett. **14**(11), 6672–6678 (2014).
16. T. Ellenbogen, K. Seo, and K. B. Crozier, "Chromatic plasmonic polarizers for active visible color filtering and polarimetry," Nano Lett. **12**(2), 1026–1031 (2012).
17. M. W. Knight, N. S. King, L. Liu, H. O. Everitt, P. Nordlander, and N. J. Halas, "Aluminum for plasmonics," ACS Nano **8**(1), 834–840 (2014).
18. Z. Fang, Y.-R. Zhen, L. Fan, X. Zhu, and P. Nordlander, "Tunable wide-angle plasmonic perfect absorber at visible frequencies," Phys. Rev. B **85**(24), 245401 (2012).
19. W. Cai, U. K. Chettiar, H.-K. Yuan, V. C. de Silva, A. V. Kildishev, V. P. Drachev, and V. M. Shalaev, "Metamagnetics with rainbow colors," Opt. Express **15**(6), 3333–3341 (2007).
20. N. Liu, M. Mesch, T. Weiss, M. Hentschel, and H. Giessen, "Infrared perfect absorber and its application as plasmonic sensor," Nano Lett. **10**(7), 2342–2348 (2010).
21. F. Cheng, X. Yang, and J. Gao, "Enhancing intensity and refractive index sensing capability with infrared plasmonic perfect absorbers," Opt. Lett. **39**(11), 3185–3188 (2014).
22. Q. Chen and D. R. S. Cumming, "High transmission and low color cross-talk plasmonic color filters using triangular-lattice hole arrays in aluminum films," Opt. Express **18**(13), 14056–14062 (2010).
23. M. Melli, A. Polyakov, D. Gargas, C. Huynh, L. Scipioni, W. Bao, D. F. Ogletree, P. J. Schuck, S. Cabrini, and A. Weber-Bargioni, "Reaching the theoretical resonance quality factor limit in coaxial plasmonic nanoresonators fabricated by helium ion lithography," Nano Lett. **13**(6), 2687–2691 (2013).
24. http://refractiveindex.info/
25. C. Wu, B. Neuner, G. Shvets, J. John, A. Milder, B. Zollars, and S. Savoy, "Large-area wide-angle spectrally selective plasmonic absorber," Phys. Rev. B **84**(7), 075102 (2011).
26. H.-S. Lee, Y.-T. Yoon, S. S. Lee, S.-H. Kim, and K.-D. Lee, "Color filter based on a subwavelength patterned metal grating," Opt. Express **15**(23), 15457–15463 (2007).
27. http://pixabay.com/en/art-frame-pastel-95850/

1. Introduction

Structural color filtering and printing technologies employing photonic crystals [1], plasmonic metamaterials [2–4] and metasurfaces [5–7] have recently presented great advantages over conventional colorant-based pigmentation with higher resolution [8–10], better sustainability [6], easier recycling, and lower cost. Both localized surface plasmons [5–7] and propagating surface plasmons (SPs) [2,3,8] excited on metamaterials have been utilized to create plasmonic resonances with tunable spectral responses across the entire visible spectrum for realizing various colors in either transmitted or reflected light. To date, a majority of plasmonic filtered colors are generated by noble metals such as silver [9–12] and gold [5] due to their lower ohmic losses in the visible spectrum. However, the interband transition of gold prevents rendering visible colors at the wavelength below 500 nm [5,13], while silver nanostructures are susceptible to oxidation and sulphidation which will degrade the color performance [12]. Moreover, silver is not compatible with complementary metal oxide semiconductor (CMOS) fabrication processes, which limits its practical applications [14]. Recently, aluminum has been identified as a promising substitute for gold and silver to realize plasmonic color printing [6,7,15,16], due to the outstanding optical properties of aluminum in the visible and near-UV regions in addition to its low-cost and sustainable merits [17]. Specifically, the interband absorption of aluminum releases the angle dependence of the generated colors since the dispersion curves of the propagating SPs supported by the aluminum-dielectric interface is closer to the light line as compared to the silver counterparts [7]. Furthermore, the low quality factor of aluminum plasmonic resonators introduces a lower spectral sensitivity for distinct colors and thus providing the benefit of a larger tolerance to critical-dimension control in the fabrication [6].

Although aluminum is a promising material for color printing applications, the color performance of the previously reported aluminum-based devices is still limited by one issue: the loss-induced spectrum broadening and flattening of the SP resonance observed in experiments [6,7] will not only reduce the spectral purity, but also decrease the color saturation or brightness. As a result, color mixing strategies are necessary to compensate for the reduced color purity due to the low quality factor of the SP resonance supported by the aluminum-based color printing devices [6]. Here we introduce and demonstrate a simple but efficient aluminum structural color printing platform based on a plasmonic metamaterial of near-perfect light absorption that significantly improves the color performance. The

aluminum plasmonic metamaterial is designed to have a near-perfect absorption SP resonance with a relative narrow bandwidth tunable across the visible frequency range. Moreover, although aluminum forms a self-limiting impermeable native oxide layer that affords long stability against oxidation and sulphidation, a mechanical protection layer is always desirable for ambient use in practical color printing applications. As demonstrated below, a protective transparent thin film polymer is coated on the fabricated metamaterials without significantly influencing the color performance. Instead, the observed color saturation is significantly improved while the resonance wavelength redshift induced by the polymer layer can be easily compensated by the geometrical adjustment in the fabrication.

2. Device design and fabrication

The metal-dielectric-metal multilayers consisting of a top 30 nm aluminum (Al) layer, a 45 nm alumina (Al_2O_3) spacer and a bottom 100 nm thick aluminum mirror, are deposited by sputtering on the top of a silicon wafer, at a deposition rate of 1.2 Å/sec for aluminum and 0.1 Å/sec for alumina. The designed circular hole arrays arranged in a triangular lattice with period P and hole radius r are then patterned on the top aluminum layer using a focused ion beam (FEI Helios Nanolab 600 DualBeam system) milling method. Figure 1(a) illustrates a schematic diagram of the fabricated aluminum plasmonic metamaterial of perfect absorption consisting of the three functional layers. Figure 1(b) shows a cross-section scanning electron micrograph (SEM) image of a selected sample with $P = 260$ nm and $r = 90$ nm. The presence of the bottom thick aluminum layer completely eliminates the transmittance ($T = 0$) of the multilayer structure due to the small penetration depth of light in aluminum at visible frequencies. Similar to the scenario of SP-assisted enhanced optical transmission through subwavelength hole arrays, here on the metamaterial, highly confined propagating SPs are excited by the periodic hole arrays on the top metallic layer, while the intermediate dielectric spacer functions as a bridge to couple the SPs on two opposite metal-dielectric interfaces [18] to form an optical magnetic dipole resonance [19,20]. The coexistence of both electric dipole and magnetic dipole resonances in the plasmonic metamaterials results in a matched impedance to that of free space, leading to a near perfect light absorption and a negligible reflection [21]. The triangular lattice is chosen instead of the square lattice, due to the fact that the hole arrays of triangular lattice have a larger wavelength interval between the first two SP resonances compared to that of the hole arrays of square lattice with the same lattice period [3,22]. In this way, the proposed metamaterials are able to reduce the color cross-talk between different plasmonic resonances and therefore enhance the color purity.
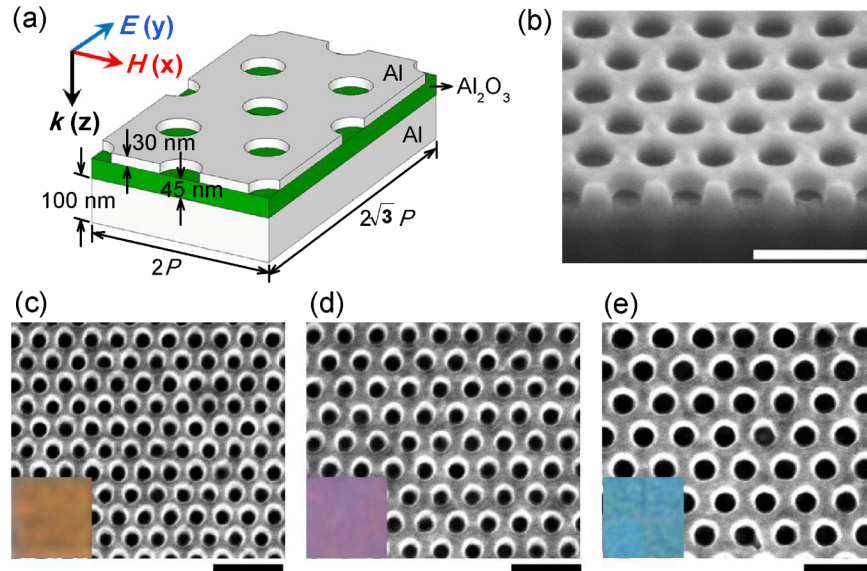
Fig. 1. (a) Schematic of four unit cells of the circular hole arrays of triangular lattice fabricated on the Al-Al$_2$O$_3$-Al triple layer structure. (b) A cross-section SEM image of the fabricated aluminum plasmonic metamaterial with period and hole size of 260 and 180 nm, respectively. (c-e) SEM images of three samples with different geometric parameters (period and hole radius) (c: $P = 180$ nm, $r = 50$ nm; d: $P = 220$ nm, $r = 60$ nm; e: $P = 280$ nm, $r = 80$ nm). Insets: Optical reflection microscopy images of the entire 20×20 μm^2 arrays. No polarization is specified in taking the color images since the proposed structures are polarization-independent under normal incidence. Scale bars: 500 nm.

3. Optical response characterization and simulation results

Next the optical spectral response of the fabricated plasmonic metamaterials is characterized in the visible range with an optical reflection measurement setup. Each fabricated sample has a structural footprint area of 20×20 μm^2 that is sufficient for the reflection measurements. SEM images of three representative samples with different geometrical parameters are shown in Figs. 1(c)-1(e). Bright-field optical microscope images of these metamaterials are also presented in the insets, showing a high degree of color homogeneity and saturation for the three primary colors of yellow, magenta and cyan in the CMY color system. Six plasmonic samples consisting of the same triangular lattice with a constant period ($P = 260$ nm) but different hole radii ($r = 60$ to 110 nm) are fabricated and characterized in order to investigate the effects of hole sizes on optical reflection spectra and corresponding colors. As shown in Fig. 2(a), when the hole radius increases from 60 to 110 nm with a 10 nm step, the resonance wavelength is blue-shifted almost linearly from 645 to 500 nm while the measured reflectivity decreases gradually from 0.42 to 0.20. A plasmonic resonance with the absorption of about 80% is observed around the wavelength of 580 nm for the sample of $r = 90$ nm, which shows a relative large intensity contrast of about 0.4 and a narrow full-width at half-maximum (FWHM) of approximately 110 nm, giving rise to a quality factor of about 5 [23]. The bright field optical image corresponding to each sample is also shown in the inset along with the measured reflection spectrum. It is noted that the color changes gradually from light cyan to yellow as the hole radius increases from 60 to 110 nm while the large intensity contrast within a small wavelength range leads to pure colors with high saturation. The measured optical reflection spectra are verified with numerical simulations using the finite element method as shown in Fig. 2(b). Periodic boundary conditions are employed along the x and y axes in the simulations to account for the periodic arrangement of the unit cells. Perfectly matched layers (PMLs) surrounded by scattering boundary condition faces are utilized along the propagation direction (perpendicular to the planar structure) to avoid multiple reflections due to geometry

truncation. The measured permittivities of aluminum (imaginary part multiplied by factor of 2 to account for surface irregularities and additional losses induced by fabrication) and alumina employed in the simulations are obtained from the refractive index database [24] and the numerical results show good agreement with the experimental data.
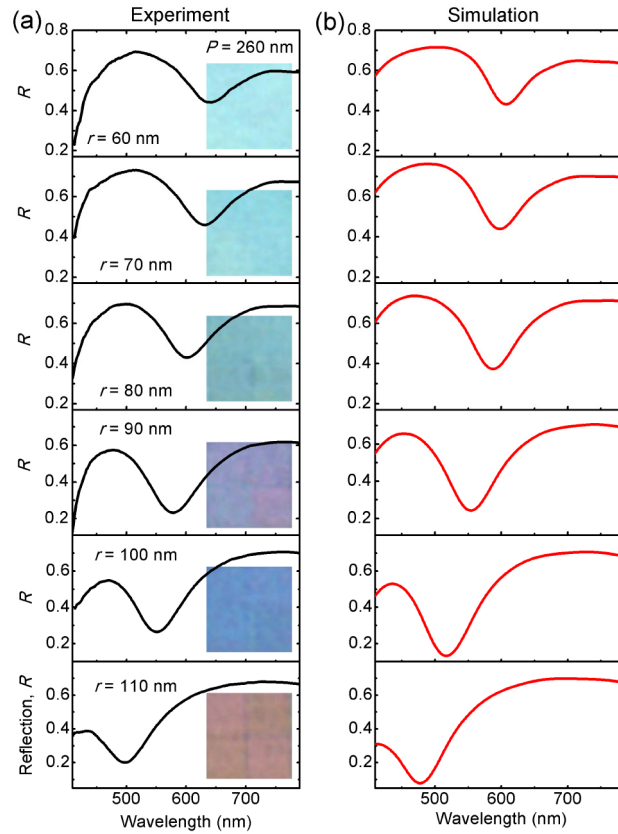

Fig. 2. Experimental (a) and simulated (b) optical reflection spectra of the metamaterials with period P = 260 nm and successively increasing hole radii (from top to bottom: r = 60 nm–110 nm) under normal incidence with linearly polarized light along the y direction as illustrated in Fig. 1(a). Insets: The measured optical images of fabricated 20 × 20 μm^2 structure.

In order to achieve a relative large tunable color gamut in the visible spectrum, the lattice period and hole radius are varied simultaneously. Figure 3(a) shows the measured (black solid curves) and simulated (red dotted curves) optical reflection spectra when the period and hole radius increase from 180 to 330 nm and from 60 to 115 nm, respectively. Period values smaller than 350 nm are chosen in order to reduce the influence of lattice diffraction and allow for wider viewing angles [5]. A rich color appearance is obtained, including three primary colors as well as the intermediate colors with good color purity and saturation. All the measured optical reflection spectra depicted in Fig. 3(a) have also been converted to the CIE 1931 chromaticity coordinates as shown in Fig. 3(c), illustrating the color gamut achieved by the fabricated metamaterials. It is shown that the measured chromaticity coordinates are all around the achromatic point, demonstrating the capability of aluminum plasmonic metamaterials for a relative large degree of color range tuning [7].

4. Optical responses modified by the presence of a protection layer

In order to use the metamaterial color printing platform in a harsh ambient environment and prevent not only chemical degradations such as oxidization and contamination but also

mechanical damage due to scratching and battering, the fabricated aluminum plasmonic metamaterials are protected by a 100 nm thick spin-coated poly(methyl methacrylate) (PMMA) layer on the top of the device. Figure 3(b) shows the measured (black solid curves) and simulated (red dotted curves) optical reflection spectra of the PMMA-coated metamaterials and respective bright-field microscope images. As compared to the optical response of bare structures shown in Fig. 3(a), the addition of the PMMA layer leads to a small redshift of the resonance wavelength due to an increase of the refractive index in the overlay material. More importantly, the magnitude of the optical reflection at the resonance undergoes a significant reduction for all the fabricated metamaterials. For example, for the sample with $P = 260$ nm, the measured minimum optical reflection intensity reduces from 0.29 at the resonance of 585 nm for the bare structure to 0.03 at the resonance of 600 nm for the PMMA-coated structure. The observed colors are also changed due to the redshift of the resonance wavelength, while the addition of protective PMMA coating improves dramatically the color saturation due to the near perfect light absorption at the resonance wavelength. A distinctly different CIE 1931 chromaticity diagram is obtained from the measured optical reflection spectra, as shown in Fig. 3(d), illustrating a larger color gamut and improved color saturation with the PMMA coating.
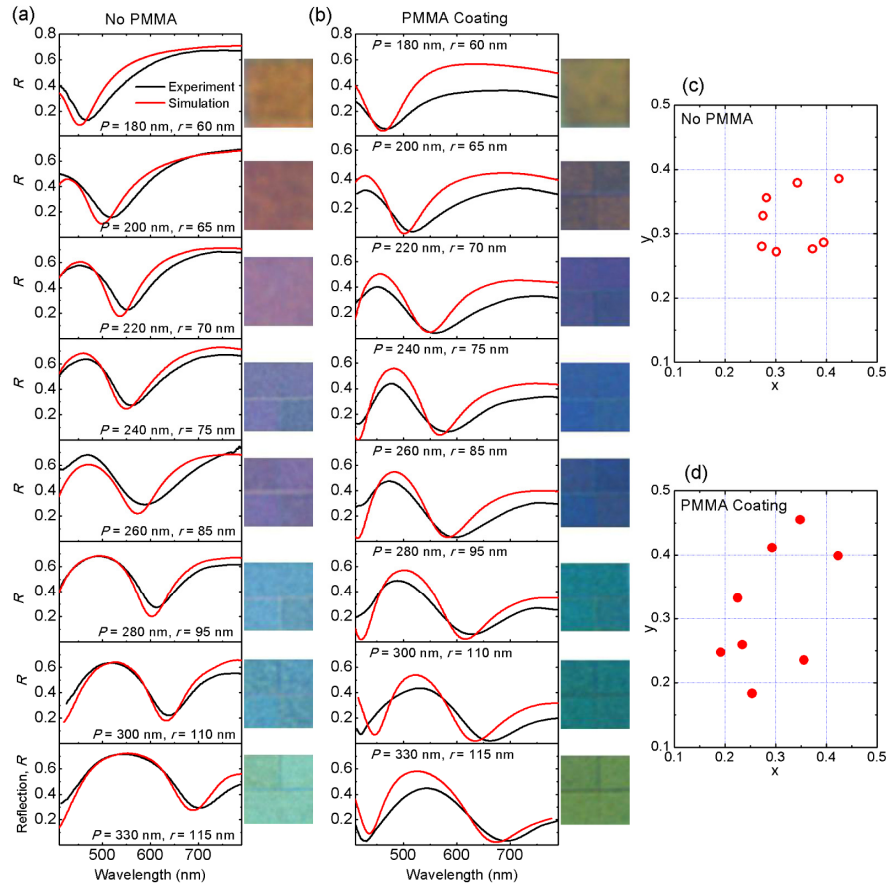

Fig. 3. The measured optical reflection spectra of the fabricated metamaterials with increasing lattice period and hole radius ($P = 180$–330 nm, $r = 60$ nm–115 nm) for both (a) the bare and (b) the PMMA-coated metamaterials under normal incidence with linearly polarized light along the y direction as illustrated in Fig. 1(a). Insets: Measured optical microscopy images of the fabricated 20×20 μm^2 structures. CIE 1931 chromaticity coordinates of both (c) bare and (d) PMMA-coated metamaterials.

In order to understand the mechanism of the stronger absorption resonance and thus the better color saturation obtained with the PMMA-coated metamaterials, the optical spectral response and electromagnetic field distributions at resonance wavelength are analyzed numerically for a selected sample with $P = 250$ nm period and $r = 75$ nm, as shown in Fig. 4. According to the plotted time-averaged magnetic field (color map) and electric displacement (white arrows) distributions in Fig. 4 (b) at the resonance wavelength λ_1 of the bare structure, a strong magnetic dipole resonance with enhanced magnetic field concentrated within the dielectric spacer is formed by the anti-symmetric current flow [19,25]. When a PMMA layer is coated on the metamaterial, a more symmetric dielectric environment is created around the top aluminum layer so that the coupling of SPs on both sides of the metal layer is enhanced [22,26]. As a consequence, a stronger magnetic dipole resonance is established for the PMMA-coated metamaterial shown in Fig. 4(c) as compared to that on the bare metamaterial shown in Fig. 4(b). Furthermore, for the PMMA-coated metamaterial, the impedance matching condition between the structure and free space is satisfied and thus near perfect absorption at the resonance wavelength is obtained. Meanwhile, a broadening of the absorption resonance bandwidth is also observed for the PMMA-coated structure (black curve in Fig. 4(a)), due to the slightly weaker confinement of the electromagnetic field within the dielectric spacer induced by the existence of PMMA coating.
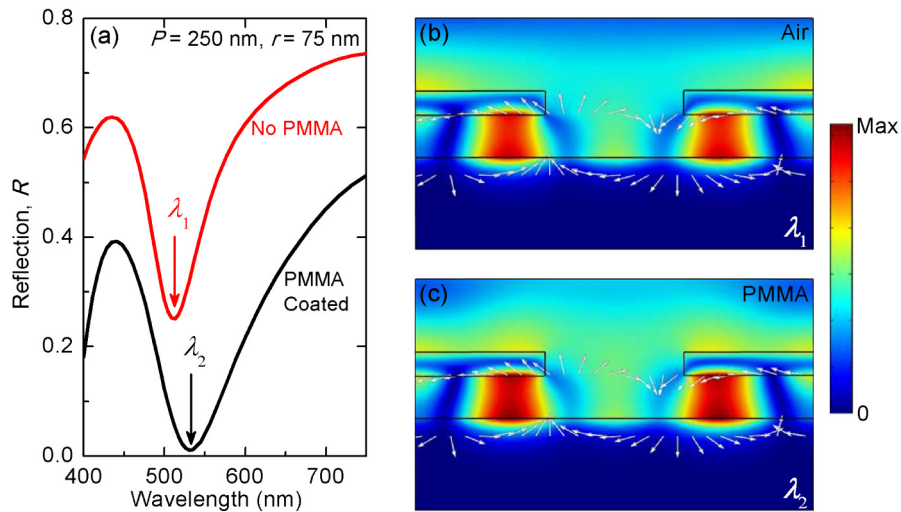

Fig. 4. (a) Calculated reflection spectra of a selected sample ($P = 250$ nm, $r = 75$ nm) with (black) and without (red) the PMMA coating under normal incidence with linearly polarized light along the y direction as illustrated in Fig. 1(a). The time-averaged magnetic field intensity (color map) and electric displacement (white arrows) distributions for (b) the bare metamaterial at the resonance wavelength λ_1 and (c) the PMMA-coated metamaterial at the resonance wavelength λ_2.

To further illustrate the effects of the PMMA protective coating on the color appearances of plasmonic metamaterials, the bright-field optical microscopy images of a series of bare and PMMA-coated metamaterials are compared in Fig. 5. The lattice period ranges from 160 to 360 nm and the hole radius increases from 40 to 120 nm in the color palette, where more than 70 distinct colors are obtained. As demonstrated above, the addition of a PMMA protection layer induces slight color variations but high color saturation or brightness on the perceived colors. The gamut of the color palette demonstrates that by the appropriate choice of lattice period and hole radius in the metamaterials, a desired color production can always be achieved with the polymer protection [5]. In order to prove and illustrate the suitability of the aluminum plasmonic metamaterials in structural color printing related applications, a micrometer-scale ($50 \times 38 \ \mu m^2$) plasmonic printed copy of a pastel painting [Fig. 5(c)] from a public domain resource [27] is fabricated and its visual performance is tested under

microscope. By choosing the appropriate lattice periods and hole radii for each color area and considering the effect of the frequency redshift induced by the PMMA layer, the desired image colors can be reproduced with a relative higher brightness and visual contrast, as shown in the image of the PMMA-coated plasmonic painting [Fig. 5(e)] with a better color fidelity, compared to that obtained for the uncoated one [Fig. 5(d)].
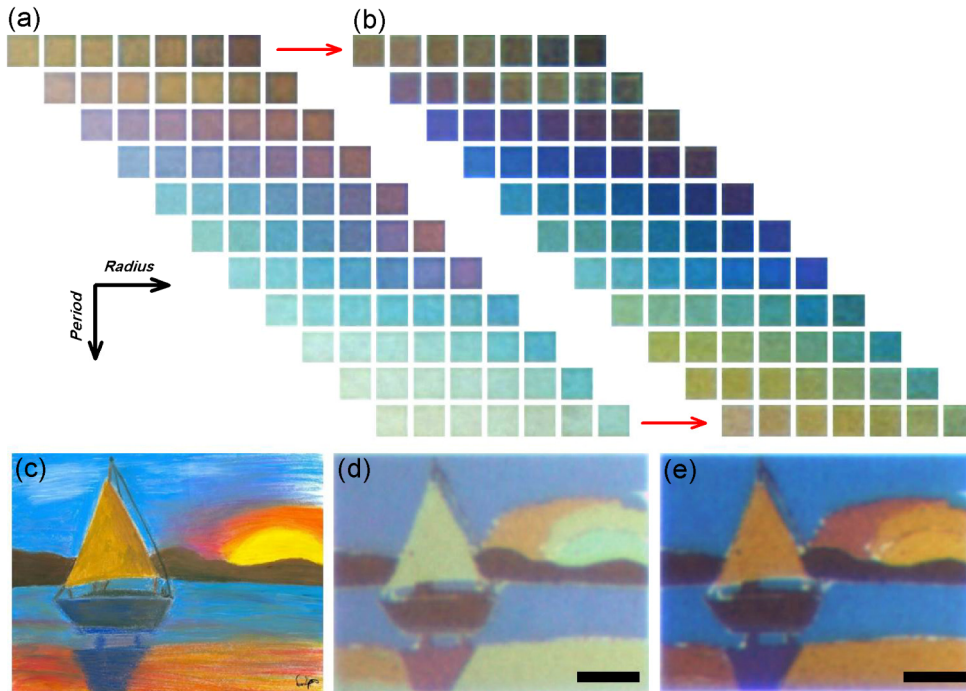

Fig. 5. (a) The measured bright-field microscope images of the bare metamaterials with period varying from 160 nm to 360 nm and hole radius ranging from 40 nm to 120 nm. (b) The bright-field microscope images of the PMMA-coated metamaterials. (c) Original image of a selected pastel painting obtained from a public domain resource. (d) The measured optical microscopy image of the uncoated plasmonic painting. (e) The measured optical microscopy image of the PMMA-coated plasmonic painting. Scale bars: 10 μm.

5. Angular dependence of optical spectral responses

Finally, the incident angle dependence of the optical spectral response is investigated numerically for a PMMA-coated metamaterial with $P = 250$ nm and $r = 75$ nm under both TE (electric field parallel to y axis) and TM (magnetic field parallel to y axis) polarizations. As shown in Fig. 6(a), the excitation of SPs via the lattice coupling limits the angle independence of the reflection spectra for TM polarization. However, the effect of lattice coupling on the reflection spectral response is much less pronounced for the TE polarization as shown in Fig. 6(b), where the minimum reflection remains lower than 5% even at large incident angles (70°) due to a strong, robust magnetic dipole resonance, although a small resonance splitting is observed at incident angles larger than 20°. The angle-resolved chromaticity coordinates under the TE polarization have also been calculated from the simulated optical reflection spectra [Fig. 6(c)], which confirms a stable color appearance under large viewing angles up to 70°.
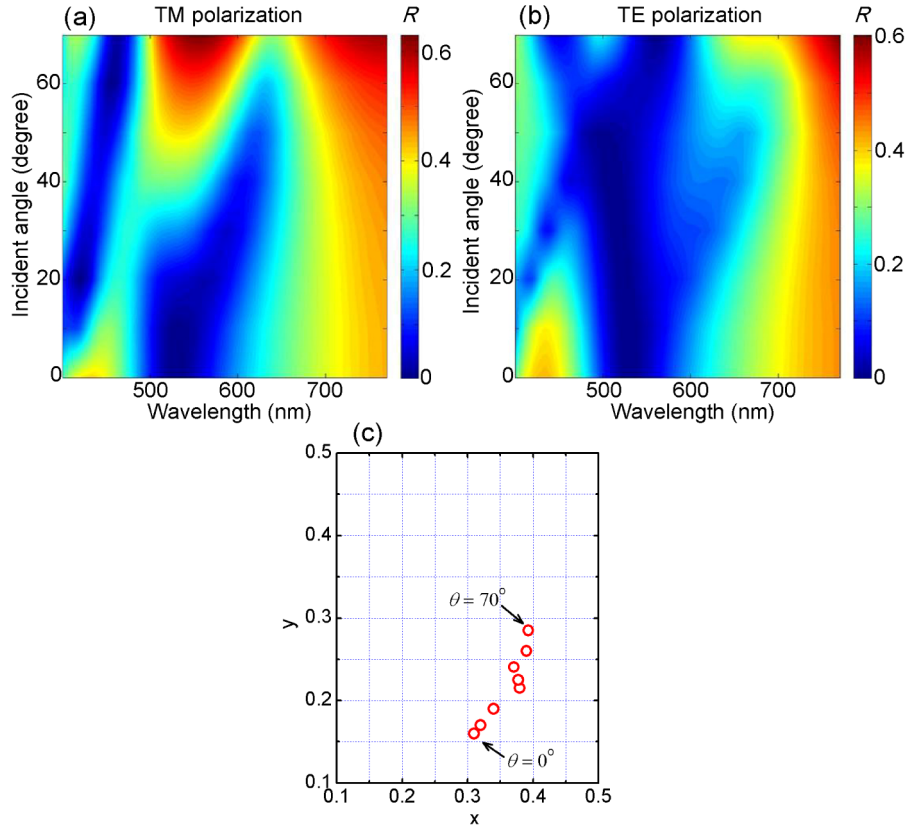
Fig. 6. Incident angle dependence of the simulated reflection spectra under the (a) TM polarization and (b) TE polarization for a PMMA-coated metamaterial with P = 250 nm and r = 75 nm. (c) Incident angle resolved chromaticity coordinates calculated from the reflection spectra under the TE polarization.

6. Conclusion

In summary, we have demonstrated an aluminum-based, high-performance plasmonic structural color printing platform with high resolution and high color saturation. Aluminum plasmonic metamaterials with single tunable resonance and near perfect light absorption across the visible frequencies have been achieved by simply scaling the lattice period and hole radius in the structure design. A protective polymer coating helps to satisfy the impedance matching to free space and thus yields pure colors with high saturation. In addition, the color performance exhibits low dependency on incidence angles under TE polarization. The demonstrated aluminum plasmonic metamaterials for structural color printing will be well suited for a wide range of relevant applications, such as anti-counterfeit tag and security marking where erosion- and friction-resistant, robust color performance is particularly important.

Acknowledgments